A micromachined thermoelectric sensor for natural gas analysis: Multivariate calibration results

S. Udina[a,c,*], *M. Carmona*[a], *A. Pardo*[a], *J. Santander*[b], *L. Fonseca*[b], *S. Marco*[a,c]

[a] Departament d'Electrònica, Universitat de Barcelona, Martí i Franquès, 1, 08028 Barcelona, Spain

[b] Centre Nacional de Microelectrònica, Campus UAB, 08193 Bellaterra, Spain.

[c] Artificial olfaction group, Institute for Bioengineering of Catalonia (IBEC), Baldiri i Rexach 13, 08028-Barcelona, Spain

NOTE FOR EDITOR / REVIEWER: PLEASE NOTE THAT REFERENCES TO FIGURES ARE ACCOMPANIED WITH AN ABBREVIATION IN CAPITAL LETTERS; THIS IS TO ENSURE THAT NUMBERS REFER TO THE RIGHT FIGURE. THEY NEED BE REMOVED BEFORE PUBLICATION.

* Corresponding author at:

Departament d'Electrònica, Universitat de Barcelona, Martí i Franquès, 1, 08028 Barcelona, Spain

Tel.: +34 93 403 91 48 Fax: +34 93 402 11 48; email: sudina@el.ub.es (S. Udina)

ABSTRACT

The potential use of a micromachined thermopile based sensor device for analyzing natural gas is explored. The sensor consists of a thermally isolated hotplate which is heated by the application of a sequence of programmed voltages to an integrated heater. Once the hotplate reaches a stationary temperature, the thermopile provides a signal proportional to the hotplate temperature. These signals are processed in order to determine different natural gas properties. Sensor response is mainly dependent on the thermal conductivity of the surrounding gas at different temperatures. Seven predicted properties (normal density, Superior Heating Value, Wobbe index and the concentrations of methane, ethane, carbon dioxide and nitrogen) are calibrated against sensor signals by using multivariate regression, in particular Partial Least Squares. Experimental data have been used for calibration and validation. Results show property prediction capability with reasonable accuracy except for prediction of carbon dioxide concentration. A detailed uncertainty analysis is provided to better understand the metrological limits of the system. These results imply for the first time the possibility of designing unprecedented low-cost natural gas analyzers. The concept may be extended to other constrained gas mixtures (e.g. of a known number of components) to enable low-cost multicomponent gas analyzers.

Keywords: Gas sensor, natural gas, MEMS, Superior Heating Value, density, PLS.

1. Introduction

Natural gas property measurement is a field witnessing a remarkable evolution over the last few years [1]. In direct relation to gas market liberalization within the European Union, triggered by the regulation framework known as the 'EU Gas directive' in 1998 [2], gas properties are expected to vary more frequently and more strongly. Precise monitoring of these variations is of great economic and technical importance.

Natural gas consists mostly of methane with lesser amounts of ethane and propane. Non-combustible components such as carbon dioxide and nitrogen may also be present. The higher hydrocarbons (C4 and greater) typically comprise less than 1.5 mol% of the total. In general, methane does not fall below 86 mol% while ethane and propane do not exceed 10 and 2 mol%, respectively [3]. Carbon dioxide and nitrogen typically do not exceed 2 and 12 mol% respectively [4, 5]. This variability in composition causes significant variations in natural gas properties, for instance of up to 25% for Superior Heating Value (33-44 MJ/m^3 [6]), Wobbe index (42-56 MJ/m^3) and normal density (0.7-0.93 Kg/m^3). These properties are usually calculated from the concentrations by use of the ISO6976 standard [7], developed specifically for this purpose.

. Natural gas properties are closely monitored in several scenarios, for instance in commercial transactions, gas processing and storage, and also in process and engine control. In these applications, measurements of the heating values (superior and lower), normal density, specific gravity, compressibility factor, index [7] or Methane Number [8] among other magnitudes, are needed. Among the natural gas properties, the heating value (in its various definitions [7]) is probably the most relevant one, for it is a measure of the energy content, and has significant economic implications. Several methods have historically been proposed to monitor this property [1, 9-11]. Few of these methods have been widely accepted in the industry given its typically stringent reliability requirements and regulations. A first generation of industrial devices comprised diverse types of combustion calorimeters [10]; these were largely substituted by a second generation of devices, the Process Gas Chromatographs (PGCs) [9]. Currently a third generation of faster and lower-cost devices is being progressively introduced in the

industry. These devices are based on correlative methods [1, 12, 13]. The term 'correlative' makes reference to the fact that they mathematically correlate a set of selected, easier to measure, physical measurements with the properties of interest. The chosen physical measurements vary in each case but include combinations of thermal conductivity measurements, NDIR (Non Dispersive Infrared) absorption [12], speed of sound [14], carbon dioxide molar fraction, viscosity and others [1]. These third generation devices will probably complement the PGCs, rather than fully replace them. This is due to their lower accuracy (indeed they are usually calibrated against PGC measurements). Nonetheless price range, bulkiness and/or maintenance needs of these devices still render the ideal situation of a low-cost and real-time domestic and industrial gas quality meter as a challenge beyond the state of the art.

The present work takes a significant step towards this direction by presenting natural gas analysis results based on measurements taken by a single microsensor. The measurement principle is based on the thermal conductivity of the gas, which is dependent on the gas composition.

The use of thermal conductivity for gas analysis dates as far back as 1880 according to Weaver[15], and though other technologies have arisen and found wider application, the fact is that some of the mentioned correlative gas analyzers make use of it [12, 13], though always in combination with other measurements.

Rahmouni et al. [5,16] reported around 2003 two works showing the possibility of using only thermal conductivity measurements to infer natural gas properties such as Wobbe index (W) and Superior Heating Value (SHV or H_s), with moderate uncertainty (of around 1%). In these works, a series of measurements were performed with a setup based in two cylindrical chambers stabilized at different temperatures and including a thermal conductivity sensor each. The present work takes an important step forward with the use of a single thermoelectric sensor [17], with an embedded heater, a single measurement chamber and no gas thermalization, in combination with chemometrics, to infer the natural gas properties. This approach has a strong impact in size, mechanical simplicity and cost reduction.

The field of microsensors for gas analysis has evolved considerably over the past years, in a majority of cases involving reactive transduction processes providing high sensitivity [18,19] but also low

selectivity, a fundamental characteristic in the field of electronic noses [20,21]. Poor selectivity is usually improved with the use of sensor arrays, temperature cycling, and signal processing which are fundamental techniques in the field of electronic noses and in general chemical sensor arrays; an extensive and comprehensive review of such approaches can be found [22]. It is well-known that systems involving reactive transduction suffer in many cases from poor stability over time [23,24]. It has been proposed that a compromise arises between sensitivity and reversibility [22]. Furthermore, reversibility is directly related with sensor signal stability. Most of these microsensors for gas analysis work at high temperatures to enhance, or even enable, the reactive transduction processes. As a consequence, a widely adopted configuration for this type of sensors is the deposition of a chemically sensitive layer on top of a micromachined hotplate [25-29].

The present work is in closer relation to other microsensing approaches which do not involve a reactive process, and respond to the change of thermal transport properties of the surrounding gas (thermal or passive sensors), as is the case in thermal conductivity based microsensors, which have already been proposed in scientific publications and patents [30-32], and have been specially successful in the field of detectors for gas chromatography [33,34] This type of sensors can be considered as having low sensitivity in exchange for high reversibility.

Regarding the particular field of natural gas, Puente et al. [35] reported a thermal microsensor intended for Methane Number determination, but slow response time limited the applicability of the device. The fact is that though thermal microsensors have been successful in many applications, in the field of gas sensing these have remained widely ignored to date, finding only limited applications in the resolution of binary gas mixtures and Pirani gauges [36]. Comparable micromachined thermal sensors have been introduced as detectors in Micro-GC instruments, but in this case, the chromatographic column provides analyte separation. In such conditions the GC detector is in fact analyzing an ideally binary mixture (carrier + analyte) at every point of the elution profile [34]. This latter case is thus similar to other binary mixture measurement approaches. Binary mixtures analysis is a much simpler problem

from a signal processing point of view but much more complex for measurement setup (in the case where a chromatographic separation has to be used), compared to the presented work.

Natural gas properties measurement is a field requiring not very high sensor sensitivity (variations in the % range) but very high sensor stability. For this reason passive gas sensors were thought to be good candidates for the application and were studied [17]. In that previous work, a candidate microsensor was presented. It was studied and characterized using experimental measurements and finite element modeling (FEM) simulations, in order to determine its potential for fast, low-cost natural gas analysis. Though the sensor consists of a commonly used thermal sensor structure [36-38], an unprecedented excitation mode of the sensor heater allows obtaining measures which are related (indirectly) to the thermal conductivity as a function of temperature, k(T). However, extracting this information from the sensor measurements is a demanding task in the signal processing stage due to its high sensitivity to undesired interferences (ambient temperature, pressure, and noise in the heater excitation voltage) and the small changes in $k(T)$ to be detected.

To the best of our knowledge this is the first work reporting the assessment of properties and composition of a multi-component (of more than 2 components) gas mixture using only a single thermal microsensor.

The paper is organized as follows. A brief sensor description is provided in section 2 which also summarizes relevant previous work [17]. After that the materials and methods section (section 3) describes the experimental and simulation setups, the signal processing and validation procedures. Section 3 also briefly presents a highly relevant uncertainty analysis, the details of which are described in appendix A at the end of the paper. The results and discussion section (section 4) provides the quantitative results for the prediction models and the uncertainty analysis, and also the discussion of the results of the work. Closing the paper, conclusions are drawn in section 5.

2. Sensor description

The sensor is based on measuring the differential temperature increase between a hot spot in a micromachined membrane and the silicon rim acting as a heat sink. The temperature of the hot spot is increased by an integrated resistive heater. Similar sensor configurations have been reported for infrared sensing [38] or microcalorimetry [39]. A top view of the device can be seen in Figure 2 in reference [17].

The device studied in this work has been fabricated with CMOS compatible micromachining processes. This has many advantages, like the possibility to integrate electronic signal acquisition and conditioning in the same chip, enhanced sensing properties, on-line metering, quick response times as well as achieving low power consumption.

The sensor structure consists of a thin membrane defined on a silicon chip, as seen in Fig. 1 in reference [17]. The membrane is a 1500 × 1500 μm^2 multilayer sandwich structure of SiO_2/Si_3N_4 which sustains the thermocouple stripes extending from the silicon rim (where their cold junctions stand) to a hotplate in the center of the membrane (where the hot junctions lay). The device has 10 thermocouples per side, for a total of 40. A polysilicon heater is located in the hotplate to heat up the hot junctions to a desired temperature. Heater dimensions are 366 × 310 μm^2 and the total hot spot area is 450 × 450 μm^2. The backside of the die is attached to a metal casing (TO-8) using a high thermal conductivity epoxy adhesive. The metal casing acts as a heat sink to keep the substrate and rim temperature approximately at ambient temperature. The TO-8 casing includes a drilled hole in the area right below the membrane, which improves gas exchange with the surrounding atmosphere. A photograph of the encased sensor can be seen in Figure 1(SP).

Insert Figure 1 (SP) here

The choice of the thermocouples materials is of key importance since they determine the sensor performance. In fact a compromise arises between a high Seebeck thermoelectric effect and the quality

of the structure's thermal behavior [40,41], in terms of thermal conductance and overall thermal noise. The selected materials were aluminum and n-doped polysilicon. Though these materials do not provide the best thermoelectric performance, they increase CMOS compatibility and thus simplify the fabrication process.

The measurement principle consists of heating the hotplate by applying a voltage at the heater, producing a temperature distribution across the device geometry. The heat generated flows through the surrounding gas, as well as through the membrane. The temperature reached at the centre of the membrane depends on the heat dissipation to ambient, which is in turn modulated by the thermal conductivity of said surrounding gas. The sensor stationary signal output is given by:

$$V_{out} = nS\Delta T \qquad (1)$$

Where n is the number of thermocouples in the thermopile, S is the Seebeck coefficient and ΔT is the temperature difference between hot and cold junctions of the thermopile. ΔT is modulated as previously described by the surrounding gas thermal conductivity $k(T)$.

The thermal isolation of the membrane and the high thermal conductivity of the silicon bulk are of great importance in order to enhance the temperature difference between hot and cold junctions. The approach is similar as that of thermal conductivity detectors [33] (TCDs) used in Gas Chromatography (GC), but without the presence of a specifically designed fluidic channel. The use of a thermopile to measure the temperature instead of measuring the heater resistance, as done in most TCDs, allows for better resolution and for a differential measure that partially rejects variations of room temperature.

The sensor output is a vector of measurements obtained by applying a voltage waveform to the sensor heater. A stationary output voltage is obtained as a sensor output response for each heater voltage and the full set of sensor output responses is defined as the output vector. This excitation-reading method provides a way to capture information about the thermal conductivity of the surrounding gas at different temperatures. Complete details on sensor characterization were already described elsewhere [17].

3. Materials and methods

This work makes use of two sets of data, a set of experimental results obtained in laboratory conditions, and an additional set of computer finite element modeling (FEM) simulation results. The first set is used for the main discussion and performance analysis, while the second set is used to complement the knowledge of the sensor operation, performance, and metrological limits. For both measurement sets, the sensor output is modeled using Partial Least Squares (PLS) [42] and a regression model is computed in order to predict natural gas properties from the sensor data in real-time (see section 3.3 for details). In order to perform a detailed error analysis a Monte Carlo analysis was set up, with synthetic noise addition to the experimental data.

A description of the simulation and experimental setups is provided next, as well as the signal processing and model validation methods. Additionally, the uncertainty and performance limits analysis are introduced, which aim to bound the expected performance of the sensing principle as well as providing some quantitative insights in the sensor operation and its uncertainty sources. The detailed description of the uncertainty analysis has been placed in Appendix A to keep the conciseness and continuity in the description of the main work.

No direct measurement is available for three of the modeled properties: normal density, Superior Heating Value and Wobbe index. In these cases, calculations were based in the ISO6976 [7] standard which provides guidelines to calculate them from a known composition. This standard is widely known and used in natural gas industrial metering.

3.1 Simulation setup

Simulated measurements have required the construction of two different models. The first model is a FEM model of the sensor device which reproduces the sensor thermal response to the electrical stimulation of the heater [17]. The modeled device reaches a steady-state temperature distribution which is dependent on the surrounding gas. For the purpose of these simulations, the gas is strictly defined by

its k(T). A second model is also needed, since the input variables of the simulation need to be the concentrations of individual natural gas main components (see experimental setup).

In order to include a given gas mixture (characterized by its composition) into the FEM model of the sensor, the characteristic k(T) curve of the gas mixture has to be computed. This is not a straightforward calculation since only approximate solutions are available to the problem of calculating the k(T) curve of a gas mixture. A common approach is the use of the equation of Wassiljewa [43].

More details on the simulation setup can be found in the first part of the previous related work [17].

3.2 Experimental setup

In order to determine the properties of natural gas, previous works [13,16] made use of the assumption that natural gas can be modeled as a three or four component mixture, with an acceptable loss of accuracy in the properties estimation. Following this approach, a gas mixing station was specifically configured to deliver controlled mixtures of four of the natural gas main components: methane, ethane, nitrogen and carbon dioxide. It was expected that results with this four component mixture could be extended to other generic compositions. Figure 2(S1) shows the configuration of the synthetic natural gas generation setup. Model 5850E mass flow controllers from Brooks Instruments were used. Bottles of pure gases Methane (*Carburos Metálicos*, 99.995 %purity), Ethane (Air products, 99.5% purity), Carbon dioxide (*Carburos Metálicos*, 99.2 % purity) and Nitrogen (laboratory line, 99.5 % purity) were used.

Insert Figure 2 (S1) Here

A total 500 ml[1]/min flow of the synthetic natural gas was supplied to a sensor chamber. After 11 minutes the concentration inside the chamber was stable (as explained in section A.3), and the flow was stopped to perform a measurement of the sensor response in static gas conditions. The gas was supplied at room temperature and atmospheric pressure. Expected accuracy of the volumetric gas composition,

[1] Referenced to IUPAC standard conditions

with the gas mixing setup, were absolute concentration uncertainties (95% confidence interval) of 0.06% in CO_2, 0.16% in C_2H_6, 0.26% in N_2, and 0.40% in CH_4 (Calculation of these uncertainties is explained in section A.3).

It is important to note that derived magnitudes and properties calculations were referenced to standard conditions of the natural gas. This is particularly relevant when calculating the SHV, normal density and Wobbe index from ISO6976 [7], since these values were used as calibration data for the prediction models obtained from the sensor measurements.

A 34970A multimeter (Agilent technologies, CA, US) sampling at 25 Hz was used to measure the voltage output of the sensor. An HM8142 programmable waveform generator (Hameg Instruments, Germany) was used to supply the voltage waveform, with a specified uncertainty in the voltage output of 0.2% of the setting. However the truly relevant specification to evaluate the consistency of calibrations across different measurement runs is the voltage setpoint repeatability instead of total setpoint uncertainty. No repeatability data is provided by the manufacturer, so it was experimentally measured and estimated at 1.2mV, and basically independent of the voltage setpoint (0.004% of full scale). This results in a considerably lower noise specification and is in good agreement with the measurement results.

The stimulation of the sensor heater was done by programming the HM8142 with a voltage steps train. The excitation waveform is shown in Figure 3(HW), together with an example sensor response to pure methane. Heater voltage levels span from 0.5V to 7V in 0.5V steps, with a step duration of 500ms, as shown in Figure 3(HW). The complete excitation cycle takes 7 seconds. Note how the sensor output is stable after approximately 150ms (T90 around 100ms), which implies that the excitation time may be easily reduced to 3 seconds. Sensor output is usually comprised in the 0-1V range under normal working conditions. At the limit condition of V_{Heater} = 7V a maximum temperature of the device of approximately 200ºC is expected under normal operating conditions, this temperature is safely below the three critical temperatures which are:

- the auto-ignition temperature of methane at 595ºC;

- the Al-Si alloying temperature, starting at 400ºC;
- Typical Aluminum annealing temperatures, which can be as low as 300ºC.

Insert Figure 3(HW) here

The synthetic natural gas mixtures used for calibration and validation are described in Table 1(XC). In order to define the measuring points, experimental design, data from literature [5] and analysis certificates kindly provided by ENAGAS LNG regasification plant in Barcelona were considered. Pure methane (99.995 % purity) was added as an additional measurement point for convenience, as it is a high precision point with lower cost compared to gravimetric mixtures.

Insert Table 1(XC) here

3.3 Signal processing

Rahmouni et al. [5], measured the actual values of the thermal conductivity of the natural gas mixtures using appropriate instrumentation, and suggested a graphical resolution method, providing interesting results. In this work however, the estimation of the thermal conductivity at a particular temperature is avoided, as it can introduce additional errors in this case. The microsensor output is a value which directly contains information of a portion of the *k(T)* curve ranging from the maximum temperature to roughly room temperature corresponding to the first excitation step. For this reason, techniques from the chemometrics field, that are suitable for extracting the chemical information even in poor signal conditions (in this case, noise and high correlation among sensor steps) have been chosen. Among the full set of techniques, for reasons of improved flexibility, scalability and applicability, Partial Least Squares (PLS) [42] was selected.

PLS regression was performed for the experimental and simulated data. The reported results were obtained with data pre-processing consisting of extracting the stationary part of the sensor response for every voltage step (four measurements of the flat region were averaged) and mean centering the data.

Measurements were used to build PLS prediction models for seven properties, four of them the individual gas concentrations of CH_4, C_2H_6, CO_2 and N_2, and three relevant properties namely: the normal density, the Wobbe index (W) and the Superior Heating Value (SHV) of the gas mixture. As

previously mentioned, ISO6976 [7] was used to derive the Wobbe index **W**, the normal density **d** and the Superior Heating value $\mathbf{H_s}$ (on a volumetric basis) of the gas from its composition.

For clarity, and in order to discuss the effect of the error sources, it is convenient to recall two basic equations of multivariate linear regression, which basically correspond to the operation (or prediction) phase and the calibration (or modeling) phase.

The inverse linear regression

$$y_{pred} = \mathbf{x}^{\mathbf{T}} \cdot \mathbf{b} \qquad (2)$$

where y_{pred} is the predicted value of a property of interest, **x** is the input vector of measurements, and **b** is the regression model, a set of regression coefficients obtained by a particular calibration procedure. Scalar *e* is the residual of the prediction.

Equation (2) shall be calculated in real-time when the system is operating in the normal operation mode. Calculation of the model, contained in the **b** vector, can generally be expressed as

$$\mathbf{b} = f(\mathbf{X_{cal}}, \mathbf{Y_{cal}}) \cdot \mathbf{Y_{cal}} \qquad (3)$$

Where $\mathbf{X_{cal}}$ is the array of experimental measurements (the sensor readings) used for calibration and $\mathbf{Y_{cal}}$ the corresponding values of the properties of interest we want to model. If it is intended to model a single property, **Y** becomes a vector, **y** (the known values of the property of interest for each gas sample). Function *f* represents the calibration procedure and is a function of the experimental calibration measurements, $\mathbf{X_{cal}}$ and its corresponding values of the properties to be predicted, y_{cal}. In our case this function is the PLS procedure, so we shall write it as f_{PLS}. So in the particular case considered here, equation (3) becomes:

$$\mathbf{b} = f_{PLS}(\mathbf{X_{cal}}, \mathbf{y_{cal}}) \cdot \mathbf{y_{cal}} \qquad (4)$$

Note that equation (4) is computed once in the calibration mode of the system, before going into operation mode. A system might not enter again in the calibration mode, unless a recalibration procedure is performed.

3.4 Uncertainty analysis

A detailed analysis of sources of uncertainty and the propagation to predictions has been performed. First, the different uncertainty sources are presented in this section and divided in two main categories: error propagation during operation mode and error propagation during calibration mode (note that they are ordered in increasing order of error analysis complexity, but in reversed time order as operation mode is entered after calibration). After that, the expected magnitudes for the different error contributions are presented as subsections. Results for error propagation and its influence on the performance of the system are provided and discussed in the results and discussion section.

Considering the operation phase (equation (2)) the total error in the prediction stage has two independent contributions: the error due to the new measurements $\boldsymbol{\varepsilon}_{\mathbf{x}}$ and the error due to the calibration $\boldsymbol{\varepsilon}_{\mathbf{b}}$, as in equation (5).

$$\varepsilon_{y_{pred}} = \sqrt{(\boldsymbol{\varepsilon}_{\mathbf{x}} \cdot \mathbf{b})^2 + (\mathbf{x} \cdot \boldsymbol{\varepsilon}_{\mathbf{b}})^2} \qquad (5)$$

The errors contributing to the uncertainty in the sensor measurement vector **x** can be listed in the first place as the uncertainty sources (or noise) affecting *sensor measuring point reproducibility* (see appendix A), which are

- Heater voltage reproducibility,
- Ambient temperature,
- Sensor intrinsic noise,
- Voltage acquisition noise,

- Aging, sensor degradation.

A second group of uncertainties affecting **x** can be described as uncertainty sources affecting *gas mixture thermal conductivity*, which are

- Ambient temperature (again, but considering its effect on the gas, not on the sensor),
- Gas pressure (may be affected by ambient pressure),

During operation mode, the regression model vector **b** is constant, $\boldsymbol{\varepsilon}_{\mathbf{b}}$ is a fixed contribution to the prediction uncertainty, and the prediction cannot get any better than $\mathbf{x} \cdot \boldsymbol{\varepsilon}_{\mathbf{b}}$.

Considering calibration mode, it is intrinsic to the multivariate calibration process that determination of the **b** vector in the calibration mode is unavoidably flawed by the system uncertainties, as can be deducted from equation (3). Equation (6) shows the propagation of errors in the **X** matrix of calibration measurements and the **y** property calibration values vector to the regression model vector **b** in an explicit way.

$$\varepsilon_{\mathbf{b}} = \sqrt{\left(\frac{\partial \mathbf{b}}{\partial \mathbf{X}} \cdot \boldsymbol{\varepsilon}_{\mathbf{X}}\right)^2 + \left(\frac{\partial \mathbf{b}}{\partial \mathbf{y}} \cdot \boldsymbol{\varepsilon}_{\mathbf{y}}\right)^2} \qquad (6)$$

This equation illustrates the propagation of uncertainties in the calibration mode.

It shall be noted that uncertainty in **b** ($\boldsymbol{\varepsilon}_{\mathbf{b}}$) has a direct contribution from uncertainty in the $\mathbf{y}_{\mathbf{cal}}$ property ($\boldsymbol{\varepsilon}_{\mathbf{y}}$) calibration values vector. Errors in $\mathbf{X}_{\mathbf{cal}}$ (the full calibration measurements set), which are logically the same as in $\mathbf{x}_{\mathbf{cal}}$ (a single measurement), are basically identical as detailed in the operation mode. Errors in $\mathbf{y}_{\mathbf{cal}}$ have different sources and correspond to those uncertainties affecting the *effective gas mixture composition*, namely:

- Mass Flow Controller (MFC) uncertainty,

- Uncertainty about the completeness of the gas replacement inside the sensor chamber (gas exchange dynamics), and

- Possible leaks or contamination of gases.

These error sources are discussed in detail in appendix A (section A.3).

Note that an additional grouping of error sources as *differential* and *common mode* errors is provided in 3.6 in order to ease the discussion of the performance limits of the system.

3.5 Validation

The Prediction error of the PLS models and other figures of merit were estimated using a test set validation with hold-out. Two datasets, of 20 calibration points and 18 validation points were used. Calibration and validation datasets are displayed in Table 1(XC).

For the simulation data, the same concentration points in Table 1 were simulated. This allows for a better matched comparison with experimental results. Larger simulation datasets were also used for extended interpretation of the sensor response modeling, and also to estimate the influence of the presence of propane in the natural gas mixture.

The number of latent variables to build the prediction models was selected by inspecting the residual validation variance, which has been calculated using equation (7)

$$R_{\text{var}}^{val} = \frac{\sum_{i=1}^{n} \left(y_{val}(\mathbf{X}) - \hat{y}_{val}(\mathbf{X}) \right)^2}{\nu} \qquad (7)$$

Where y is the measured experimental point, $\hat{y}$ is the predicted model output for a given X, and ν is the number of degrees of freedom calculated as the number of points n minus the model parameters or latent variables (LV) p. Direct visual inspection of Fig. 4(RV) displaying the normalized residual variance for the obtained prediction models, provides a simple and consistent criterion to select the number of latent variables for each model, by choosing the number of LVs which minimizes the residual variance in the validation set.

In order to evaluate the performance of the system, a number of figures of merit for the different measured variables will be presented, in particular:

- The absolute concentration error (in %) for each of the synthetic natural gas components.
- The relative error (relative to expected true value) in the normal density, Superior Heating Value and Wobbe index.

These figures of merit were calculated for the experimental and the simulation data, for comparison.

It must be noted that for simulations, in absence of experimental noise, residual variance decreases monotonically when the number of latent variables is increased. Each latent variable can be seen as an underlying layer of information of decreasing magnitude extracted from the data. As more latent variables are considered the probability that experimental noise is masking the information needed to calculate that LV (in a real-world situation) increases. Figure 5(RV) shows two SHV residual variances, one for the experimental model and another one for the simulation results.

3.6 Performance limits estimation

An expected SHV prediction performance for different experimental situations has been estimated by adding synthetic noise to the simulation results.

In order to characterize different amounts of added synthetic noise, a *differential error factor* has been introduced which simulates possible experimental situations. To understand this characterization it is convenient to split the X-block uncertainties into two categories:

- Common mode uncertainties which are ambient temperature and pressure variations. These affect simultaneously (and with high correlation) all the steps of the sensor output waveform.

– Differential error uncertainties which are heater voltage noise, voltage acquisition noise and sensor intrinsic noise (thermal noise). These affect independently (in an uncorrelated way) each of the steps of the sensor output waveform.

The *differential error factor* is defined as a proportionality factor which has been applied to the differential error sources to display its influence in SHV prediction. Results are plotted and discussed in section 4.3.

4. Results and discussion

4.1 Calibration and validation results

As described in the materials and methods section, seven PLS regression models were computed using the experimental data. The normalized residual variance of each model is shown in Figure 4(RV); the number of latent variables for each model was selected according to these results.

Insert Figure 4(RV) here

It can be seen that five of the models perform best considering two LVs, and two of them improve slightly when considering a third LV.

Residual variance values have been normalized to the squared full-scale range of the predicted properties, this normalization allows model performances to be compared in the same graph. Curves in Fig. 4(RV) provide information about which prediction models perform better, the graph is in concordance with the figures of merit in Table 2(FM), which is discussed below, for instance in that methane and normal density predictions are the best performing ones.

An additional bold solid line is displayed which corresponds to simulated data. This solid line gives information about expected model performance in theoretical absence of experimental noise.

Residual variance for the carbon dioxide reveals the low quality of the model fit, reflecting mainly experimental noise.

One relevant effect can be pointed out from the simulation results shown in Fig. 4(RV) (solid line). The performed measurements correspond to a four component mix (it has three effective degrees of freedom). However, more than three LVs provide improved calibration models according to simulation results. The reason for this is that the regression problem is slightly non-linear, and higher LVs contribute to linearize the input and output spaces. This non-linearity was hinted in previous simulation

results and is masked in the experimental measurements by noise. In accordance with this, none of the prediction models showed a performance improvement for models of more than three LVs.

Figure 5(PM) shows the prediction models for the concentration of three individual components, and for normal density, Wobbe index and Superior Heating Value. Calibration points are indicated in grey and test set validation points in black. It can be observed that prediction of methane is accurate, nitrogen and ethane can be predicted with slightly impaired accuracy, but prediction of carbon dioxide was not effectively possible. The reason for this is that variation of CO_2 in the different mixtures is small compared to the other gases, and also its thermal conductivity as a function of temperature curve is highly correlated to that of nitrogen. A clear relation can be drawn with results in Fig. 4(RV) showing that two latent variables hold most of the information for almost all models, instead of the *a priori* expectation of three (the number of degrees of freedom in the gas mixture). Information about CO_2 concentration apparently lies under the noise level for this experimental setup. Prediction of the carbon dioxide concentration is a problem commonly tackled in instruments based on correlative methods by use of NDIR measurements [1]. This option was discarded in this work to keep the many advantages of the single microsensor approach.

Insert Figure 5(PM) here (full page format suggested)

For the other three properties of interest, normal density, Superior Heating Value and Wobbe index, results show good performance of the prediction models, particularly in the case of normal density. Figures of merit of all the models are summarized in Table 2(FM).

Insert Table 2(FM) here

Table 2(FM) features simulation results which can be used for comparison. The number of latent variables used is indicated in each case.

Results show that under laboratory experimental conditions it is possible to attain a remarkable accuracy in most predictions except in the case of carbon dioxide as detailed in Table 2(FM). The

system performs best at predicting methane concentration, with a 0.60% absolute error in concentration, and assessing gas normal density with a 0.82% relative error. It is of particular relevance that SHV can be determined within a relative error of 1% (all values estimated at the 95% confidence interval).

Simulation results provide an approximation of expected performances in the absence of experimental noise. It should be noted that results indicate that in order to predict carbon dioxide concentration with some accuracy, a six LV model would be needed.

Nevertheless, simulation results in Table 2(FM) have to be considered with prudence as the underlying modeling equations [17] rely on the equation of Wassiljewa to model the thermal conductivity of a multi-component gas mixture [43]; this equation is empirical and approximate. For this reason, as more LVs are considered, the reliability of the simulations (and derived calibration models) may drop.

Considering propane, another important component of natural gas, an exploratory analysis was performed using simulations in order to check its influence on the metrological performance of the sensor. A slightly impaired performance was found in moderate accuracy models (three LVs), an increased non-linearity in the sensor readings, made it difficult to get below the 1% uncertainty threshold in the SHV prediction. Given the same experimental setup and number of calibration points, the presence of typical levels of propane would be expected to degrade by about a 30% the prediction performances in Table 2(FM). By means of an increase in the number of calibration points, or an improvement in the differential experimental noise specification (more precise excitation and/or sensor reading) the system may revert to the stated performances.

4.2 Uncertainty analysis results

A detailed error analysis has been performed as described in 3.4 and appendix A. Quantitative results of the sensitivity of the sensor to every uncertainty source, at every voltage step of the sensor excitation are provided in Table 3(UR). Table 3(UR) presents detailed results, which fully characterize the sensitivity of the sensors to the different uncertainty sources, it can be seen that this sensitivity is

dependent on the heater voltage step considered. In fact, the sensor is acting as 14 different but highly correlated sensors, with different sensitivities to noise. Among the noise sources, ambient temperature variations dominate, though for the lower voltage steps, other contributions become comparable. Table 3(UR) presents the temperature induced uncertainty for a 0.2ºC variation, which is the typical temperature oscillation inside the measurement chamber for a 24h period of time. For this reason, results in table FM hold in general for daily recalibrations of the system.

Insert Table 3 (UR) here

Table 3 is basically a summary of the experimental uncertainties. It is interesting to note that the influence of the ambient pressure appears to be negligible compared with the ambient temperature, voltmeter and heater noise. This is an important result which simplifies the conception of a real measurement device, as no special pressure regulation or compensation would be needed in first instance.

Results in table 3(UR) have been analytically estimated using known specifications for the sensor and acquisition equipment, and deriving the thermal conductivity dependence to pressure and temperature from available data for methane in the National Institute of Standards and Technology (NIST, Gaithersburg, MD, USA) [44] database (see appendix A). Differential errors in table 3 contribute independently to each voltage step while common mode ones contribute in a highly correlated way. Note that differential errors may be reduced by increasing signal integration times. For the presented sampling specifications, the sensor intrinsic noise sets an uncertainty reduction limit at about two orders of magnitude. Uncertainty related to the calibration process and y block is considered in table 4.

Insert Table 4 (PU) here

A more comprehensive and concise visualization of the influence of the different uncertainty sources in the operation mode is displayed in table 4(PU). Estimated values for each of the contributions building up $\boldsymbol{\varepsilon_X}$ are provided, and also the model uncertainty $\boldsymbol{\varepsilon_b}$ values are listed. The model uncertainty $\boldsymbol{\varepsilon_b}$ corresponds to the uncertainty strictly related to the calibration process. Estimation of $\boldsymbol{\varepsilon_b}$ is done by

including all error sources, including gas concentration uncertainty $\boldsymbol{\varepsilon_y}$ in a Monte Carlo analysis. Table 4(PU) displays the influence of each noise source in the predictions, by applying the sensor output variation due to each error source as an input to the prediction model for each property. As a result, effects of the uncertainty sources are summed up for the full sensor output waveform.

The values obtained compare well with the experimental results and validation, though are slightly overestimated in the case of Superior Heating Value and Wobbe index. This overestimation has been attributed to the fact that error in the gas concentrations is lower than estimated (see A.3). The reason for this is that total uncertainty provided by the manufacturer was used instead of an experimentally estimated repeatability of the mass flow controllers. Table 4(PU) shows that error in the model (the calibration error) and prediction error are very close to each other. Recalling equation (5) it shall be interpreted that the first term containing the experimental error $\boldsymbol{\varepsilon_X}$ is almost negligible in front of the modeling error $\boldsymbol{\varepsilon_b}$. This result suggests that either error in the calibrated properties $\boldsymbol{\varepsilon_y}$, or the modeling error (affected by the non-linearity of the sensor response to changes in gas composition), or both, dominate over the experimental error $\boldsymbol{\varepsilon_X}$. Note that this result can be misleading, since the modeling can only improve if $\boldsymbol{\varepsilon_X}$ and $\boldsymbol{\varepsilon_y}$ are low enough to allow the computation of a higher number of LVs model.

This result is in agreement with the performance limits estimation in next section, and in particular with Fig. 6 (RE). However, the apparent overestimation of the error in $\mathbf{y_{cal}}$ is probably making this error source more prominent than others. As seen in the next section, results indicate that other error sources also have a strong influence on the performance.

4.3 Performance limits estimation results

Figure 6(RE) shows the relative error in SHV prediction as a function of the differential error factor, for different PLS models corresponding to 2, 3, 4 and 6 latent variables.

Results in Fig. 6(RE) are in good agreement with experimental results in Fig. 4(RV) as SHV prediction performance does not significantly improve for PLS models of more than two latent variables. Also relative error values are in close agreement with experimental results for the differential error factor of one which corresponds to the estimated real experimental noise situation.

Insert Figure 6(RE) here

As expected, PLS modeling appears considerably robust to error sources. On the other hand, getting below the 1% uncertainty seems to require a considerable effort in experimental error reduction. Even in this case the performed simulation analysis suggests that uncertainty around 0.5% is the best performance the present technological approach can render even with a costly two order of magnitude differential error reduction. This two order of magnitude differential error reduction is an approximate limit already estimated according to results in table 3. However, a significant increase in integration times (of a factor ten and above) may improve this estimation. Also a significant increase in the number of calibration points (of a factor three and above) may enable improved modeling with a higher number of LVs and thus reduce $\boldsymbol{\varepsilon_b}$.

Regarding common mode errors (pressure and temperature), simulations suggest that PLS modeling performs very well at rejecting them when they are large enough to sensibly influence the relative error figures. In particular an increase of common mode error variation by a factor of ten did not affect the prediction in a statistically significant way. Interestingly, in this latter case optimal PLS model became a three LV model. The presence of this third latent variable hints that the PLS regression was able to model and reject the very high common mode noise using this third latent variable.

Uncertainties in the Y block are due to inexact knowledge of the true gas mixture composition. They can be regarded as common mode uncertainties as they affect in a correlated way all the values of the sensor output vector. Simulation analysis hints that an error reduction in the Y block ($\boldsymbol{\varepsilon_y}$) by a factor of

ten or error increase by a factor of two does not affect prediction performance significantly after recalculation of the PLS model. This result complements the interpretation of Table 4(PU), the additional information reveals that the clear domination of the modeling error over prediction error in table 4(PU) is due to several error contributions preventing the computation of a valid (informative) third latent variable in the model (considering the SHV model). The reason of this limitation in the modeling does not seem to be mainly due to $\boldsymbol{\varepsilon}_y$ bur rather an effect of several error contributions with a particularly relevant influence of the differential error sources (described in 3.6).

Results in tables 2 (FM) and 4 (PU) offer an interesting view of the system limitations. Pressure dependence appears negligible when typical ambient pressure variations are considered. Ambient temperature, heater voltage excitation and sensor voltage reading come as the next error sources in importance. The two *differential error* sources (heater voltage excitation and voltage reading) cannot be well modeled, and thus are not rejected, by the PLS modeling. For this reason noise reduction in both measurements seems to be a first option to improve the system performance. This reduction is technically possible by improving the voltage acquisition and heater voltage generation, or by lengthening the measurement integration times.

5. Conclusions

As a general trend, the development in micro gas-sensors has lately focused on the quest for higher sensitivity and improving detection limits [22], while sensors based on thermal sensing have an intrinsically lower sensitivity. In the present application, a very high sensitivity is not needed, since the concentrations to determine are in the percent range. However, measuring the different gas properties with reliability and accuracy is of critical importance. In exchange for the lower sensitivity, an intrinsically stable and reliable sensing mechanism has been presented. Improved reliability is due to the absence of chemical interaction in the transduction process, a known cause of sensor drift and aging [22-24,45].

It has been shown that the presented thermoelectric microsensor device, in combination with PLS regression, is able to predict different properties of natural gas with sufficient accuracy. As a consequence, the reported single sensor approach opens a perspective for low-cost natural gas analyzers, ultimately enabling affordable energy consumption meters, with a dramatic cost reduction with respect to current technologies.

Though the reported accuracy attainable with this approach is clearly below that of the reference technology – PGC – it must be noted that 1% accuracy has been achieved for the SHV prediction. These results suggest that higher accuracies can be obtained by improving the measurement conditions, especially reducing differential error sources: heater voltage repeatability and voltmeter noise. Partial Least Squares modeling seems to be able to reject common mode noise such as ambient temperature and pressure even in adverse conditions.

Nevertheless, accuracies below 0.6% seem to be extremely hard to reach and can be regarded as an intrinsic limit of this technological approach. However, it is probable that an increase in the number of calibration samples may improve this system limitation. Also the use of an alternative excitation of the sensor heater with innovative techniques [46,47] may improve these limits.

A remarkable analysis time of eight seconds has been presented, but shorter analysis times are possible by optimizing the sensor excitation and/or geometry. This approach has clear advantages regarding speed, size, simplicity and cost compared to previous instrumentation alternatives. Moreover, the concept may be extended to other gas mixtures, with known number of components and concentration constraints, to enable low-cost multi-component gas analyzers.

APPENDIX A. Uncertainty Analysis

A.1 Uncertainty sources affecting sensor repeatability (X block)

The different uncertainty sources in this category group those strictly related to the sensor operation point. To clarify, if we consider an ideal case where the sensor is surrounded by a gas volume of constant thermal conductivity k (regardless of ambient conditions), all non-repeatability of the measurements would be originated by this group of uncertainties. Additionally, noise in the voltage readout has also been included in this section.

Heater voltage reproducibility has a very strong influence in the sensor performance, as the temperature difference of hot and cold junctions depends in first approximation as the square of the heater voltage as is shown in equation (A1)

$$\Delta T = R_{th}(T) \cdot P_h \cong R_{th} \cdot \frac{V_h^{\,2}}{R_h(V_h)} \qquad \text{(A1)}$$

Where ΔT is the temperature difference between hot and cold junctions of the thermopile, to which the sensor output is proportional, as shown in equation (1), R_{th} is the thermal resistance to the ambient (dissipation), P_h is the power applied to the heater element, R_h is the resistance of the heater element, and V_h is the voltage applied to the heater element. Dependence of R_{th} with temperature (and voltage) is not an effect related to the sensor operation point and only for the purpose of this discussion it will be considered a constant. Despite this assumption, it can be noted in advance that its contribution is in this case masked by the magnitude of the other terms $V_h^{\,2}$ and $R_h(V_h)$.

To estimate the uncertainty in ΔT due to noise in V_h lets first consider equations (A2) and (A3)

$$\varepsilon_{\Delta T}(V_h) = \frac{d\Delta T}{dV_h} \cong R_{th} \cdot \frac{2V_h}{R_h(V_h)} \cdot dV_h - \frac{1}{R_h(V_h)^2} \cdot \frac{dR_h}{dV_h} \cdot dV_h \qquad \text{(A2)}$$

$$\frac{dR_h}{dV} = \frac{dR_h}{dT} \cdot \frac{dT}{dV_h} = TCR \cdot \frac{d\Delta T}{dV_h} \qquad \text{(A3)}$$

Derivatives on *T and* ΔT are identical as, as one of the reference temperatures is considered to be fixed (the cold junction). *TCR* is the temperature coefficient of the resistor. Inserting the expression in equation (A3) into equation (A2), and also considering the output voltage equation (1), Propagation of the heater voltage noise to the sensor output ε_{Vo} can be obtained as in equation (A4).

$$\varepsilon_{V_o}(V_h) = \frac{dV_o}{dV_h} = n \cdot S \cdot \varepsilon_{\Delta T}(V_h) = n \cdot S \cdot \frac{d\Delta T}{dV_h} \cdot \varepsilon_{V_h} \cong \frac{2 \cdot n \cdot S \cdot R_{th} \cdot V_h}{R_h + R_h(V_h) \cdot R_{th} \cdot TCR} \cdot \varepsilon_{V_h} \qquad \text{(A4)}$$

Equation (A4) shows a main dependency in V_h in the numerator, and there is an additional dependency in the resistance heater term which can be determined considering a typical linear variation of R_h with temperature as in equation (A5).

$$R_h(T) \cong R_h^0 \cdot [1 + TCR \cdot (T - T_0)] \qquad \text{(A5)}$$

Note that equation (A5) is an approximation since $R_h(T)$ is slightly non-linear, particularly at high temperatures however, the linear approximation holds for a large temperature range [48].

Equations (A4) and (A5) provide an interesting insight into how the heater voltage uncertainty propagates to the output voltage. However, In order to determine the effective sensitivity of the sensor output voltage to the heater voltage noise the derivative dV_o/dV_h was estimated empirically from performed measurements. In particular, for noise calculations a sensitivity value has been calculated for each heater voltage step and approximated as a constant value for small variations around that heater voltage. This was a more convenient approach rather than estimating the individual contributions expressed in (A4) given the available data.

Effects of ambient temperature changes in the voltage output, can be described by equation (A6).

$$\varepsilon_{V_o}(T_a) = \frac{dV_o}{dT_a} = n \cdot S \cdot \varepsilon_{\Delta T}(T_a) = n \cdot S \cdot \frac{d\Delta T}{dT_a} \cdot \varepsilon_T; \qquad \text{(A6)}$$

Where T_a is the ambient temperature and V_o is the output voltage. Variable ε_T is the ambient temperature change, which in the presented measurement setup is considered as a very low frequency noise, in the 10^{-4}Hz range.

Estimation of dV_o/dT_a was performed using two different approaches; the first one was estimating an upper boundary for the derivative dR_{th}/dT_a. The second one was exploration with FEM simulation results. Both results were rather consistent and allowed a rough estimation of $\varepsilon_{Vo}(Ta)$. These two approaches are discussed in section A.2 as they do not refer to changes in the sensor operation itself.

In the actual context of this work, *sensor degradation* (aging) will be neglected, since no observable degradation occurred in the considered time frame.

As for the sensor intrinsic noise, only thermal noise has to be considered for thermoelectric sensors [48]. The thermal noise voltage, V_N, of a thermopile is given by the expression (A7)

$$V_N = \sqrt{4kTR_{el}\Delta f} \qquad \text{(A7)}$$

With k denoting the Boltzmann constant, R_{el} the electrical resistance and Δf the bandwidth of the measurement. Using the values: T=293K, R=12kΩ and Δf = 12.5 Hz, in equation (A7) results in,

$V_N = 49.25nV$.

The result is the standard deviation σ for the thermopile output due to thermal noise, so for the 95% confidence interval we shall consider $2\sigma \approx 0.1\mu V$.

Acquisition noise from the Agilent voltmeter is according to specifications: 0.0035% of reading plus 50 μV for a 10V full scale selection.

A.2 Uncertainty sources affecting gas mixture thermal conductivity (X block)

The *k(T)* curve for four main natural gas components is shown in figure 4 in reference [17]. As pointed before, for a given operation point of the sensor and gas mixture, two parameters may affect the thermal conductivity at each point of the gas volume: the ambient temperature, and the pressure of the gas mix. These are herein considered as the uncertainty sources affecting the gas mixture thermal conductivity.

As the sensors works in isobaric conditions, we shall for now consider only the temperature dependence of *k*, with the explicit notation *k(T)*. The gas volume exhibits a temperature gradient as depicted by Figure A1(TD). The thermal conductivity *k(T)* of a given gas mixture is determined at each point by *T(x,y,z)*. Heat dissipation by conduction occurs according to Fourier's law,

$$\vec{q} = -k(T)\nabla T \quad \text{(A8)}$$

Where $\vec{q}$ is the heat flux per unit area, *k* is the thermal conductivity, and ∇T is the temperature gradient. In the steady state, $\vec{q}$ is a constant for each point in the space, and is determined by the power dissipated at the sensor heater. The gas surrounding the sensor determines *k(T)*, and thus the Temperature distribution in the system. See Fig. A1.

Insert Figure A1 (TD) here

Integration of $\vec{q}$ flowing through the gas volume results in *Q*, the total heat flow, and $\Delta T/Q$ is the total thermal resistance R_{th}.

Ambient temperature influence at the sensor output was described by equation (A6). In the previous section, reference to two estimation methods for the estimation of dV_o/dT_a was made. These two methods are described next.

Regarding the first method, it is assumed that the main contribution to the dV_o/dT_a derivative in equation (A6) is the term depending on the thermal conductivity of the gas dR_{th}/dT_a, an upper boundary for this derivative was calculated assuming that all the gas volume is isothermally set at temperature T_h, which is the maximum temperature occurring in any point of the gas volume in a real situation. Curves of *k(T)* for natural gas mixtures are slightly curved upwards (see Figure 7 from reference [17]) which

means that variations of k with small temperature changes are stronger for higher temperatures. For these reason assuming that the whole gas volume is set at T_h renders an overestimation of $\varepsilon_{Vo}(Ta)$ which can be used as an upper boundary, and greatly simplifies the calculations, see equation (A9).

Once thermalization at T_h is assumed, $k(T_h)$ is calculated for two different T_a. Calculation is performed using currently accepted correlations for $k(T)$ [49] and available online at the NIST webpage [44]. Then, a sensitivity $V_o/k(T_h)$ is easily calculated from experimental data, though T_h has been obtained from simulation data. This procedure is equivalent to calculating equation (A9).

$$\Delta k(T_h) > \int_{T_a}^{T_h} \frac{k(T)}{dT} dT \quad \Big| \quad T_h > T_a \quad \text{(A9) 16}$$

$$\varepsilon_{V_o}(T_a) < \frac{\Delta V_o}{\Delta k(T_h)} \cdot \frac{\Delta k(T_h)}{\Delta T_a}; \qquad \text{(A10) 17}$$

Equation (A7) can be developed into equation A(11)

$$\varepsilon_{V_o}(T_a) = n \cdot S \cdot \varepsilon_T \left(\frac{dR_{th}}{dT_a} \cdot \frac{V^2}{R_h(T_h)} - \frac{R_{th}}{R_h(T_h)^2} \cdot TCR \right) \qquad \text{(A11)}$$

Where T_h is the temperature at the heater, which in practice will be approximated by $\Delta T+T_a$.

Equation (A12) shows the influence of two terms, one in dR_{th}/dT_a and the other one in dR_h/dT_a = TCR. It must be noted that equation (A10) holds assuming that the first term dominates over the second one, or at least that influence of this second term is never as great as to invalidate the calculated upper boundary. This assumption is backed up by simulation results, hinting an overestimation of $\varepsilon_{Vo}(Ta)$ in a factor of 2 for low temperatures, and of 1.5 for high ones.

The influence of ambient pressure has been estimated using the currently accepted correlations for thermal conductivity [49] and available online at the NIST webpage [44]. It is apparent from these correlations that thermal conductivity sensitivity to expectable ambient pressure variations is orders of magnitude lower than to ambient temperature variations. The extremely small variations of thermal

conductivity due to pressure changes in the 25 mbar range make the estimation of dV_o/dP_a sensible to the uncertainty in the values of thermal conductivity. Values provided in Table 3 for P noise in V_{out} have to be regarded as order of magnitude approximations, and the apparent anomalous behavior of the noise contribution is an artifact introduced by uncertainty in (and truncation of) the values of thermal conductivity used. For the purpose of this work, this noise source was neglected.

Laboratory variations of pressure and temperature have been measured and statistically evaluated for daily and monthly expected temperature variations. Values of 1ºC and 3ºC have been measured as conservative daily and monthly variations inside the laboratory. However, the large thermal mass and the partial tightness of the measurement chamber produce daily temperature variation smoothing to about 0.2 ºC, this second value has been used in adding noise to simulation results, and provide a clear consistency with experimental observations. Typical pressure variations of 25 mbar have been considered. These values are used in the estimation of uncertainties provided in the results section.

A.3 Uncertainty sources affecting gas mixture composition (Y block)

Uncertainty in the real composition of the measured gas has a critical effect in the calibration of all predicted values, since the composition is used to calculate all values using ISO6976 [7]. Precise determination of the composition of the mixture is in direct relation with the quality of the dataset used for calibration and test. Three different uncertainty sources can contribute to this effect, the first one is leaks or gas source contamination, which has been trusted to be negligible as the fluidic system was checked for leaks and it was assumed that gas bottles complied with the supplier's specifications. The second one is transient in the gas exchange dynamics inside the sensor chamber. The gas exchanging time was estimated analytically and confirmed empirically. A full (99.9%) replacement time $t_{99.9}$ of around 5 min was estimated. Measurements in this work were performed with a conservative 11 min of gas exchange time in order to minimize the error due to gas exchanging dynamics.

The third error source is the uncertainty in the MFC setpoints, which has been estimated using error propagation and relying on the manufacturer's specifications.

The concentration of component *i* can be expressed as a function of gas flows when the steady state is reached as:

$$x_i = \frac{f_i}{\sum_{j=1}^{n} f_j} \qquad \text{(A12)}$$

Where f_i is the flow rate of component *i* (in standard ml/min).

Uncertainty in each of the f_i flows is basically independent, thus error can be expressed as:

$$dx_i = \sqrt{\frac{\partial x_i}{\partial f_1}^2 + \frac{\partial x_i}{\partial f_2}^2 + \ldots + \frac{\partial x_i}{\partial f_n}^2} \qquad \text{(A13)}$$

Two different equations shall (A14) and (A15) be used for the partial derivatives by deriving equation (A12):

$$\frac{\partial x_i}{\partial f_i} = \frac{df_i}{\sum_{j=1}^{n} f_j} - \frac{f_i \cdot df_i}{\left(\sum_{j=1}^{n} f_i\right)^2} \qquad \text{(A14)}$$

Where the manufacturer uncertainty specification will be used as df_i. Proceeding similarly for $j \neq i$ we obtain:

$$\frac{\partial x_i}{\partial f_{j \neq i}} = -\frac{f_i \cdot df_i}{\left(\sum_{j=1}^{n} f_j\right)^2} \qquad \text{(A15)}$$

Applying equations (A14) and (A15) to equation (A13) allows computation of uncertainties for each of the components in the synthetic natural gas mixture. Numerical results were already provided in the experimental setup section.

FIGURE CAPTIONS

Figure 1 (SP) (COLOR REPRODUCTION ON THE WEB, B&W IN PRINT): **Sensor photograph**. Photograph of the encapsulation containing two sensors. High thermal conductivity epoxy resin is used to attach the dies to the metal casing. The area below the membrane of the sensors presents two holes to favour contact with surrounding gas.

Figure 2 (S1): **Gas mixing setup**. Schematic depicting the experimental setup to obtain the gas mixtures. Pressure regulators for high pressure at the gas cylinders outlet are not displayed. Each gas line presents a variable pressure regulator, a safety electrovalve and a Mass Flow Controller. Typical working flow of the setup is 500 ml/min.

Figure 3(HW): Heater and sensor output voltage waveforms. Heater voltage waveform, with overlapped sample sensor response for pure methane. Notice that total time of the measurement can be further optimized. Line 'HeaterV' (in black) is read in the left axis. Line 'Sensor response' (in grey) is read in the right axis. Notice how the train pulse times may be reduced without preventing the sensor from reaching a stationary voltage response.

Figure 4(RV): Residual variance of the PLS models. Normalized residual variance of the 7 prediction models as a function of the number of LVs. Values are normalized to the squared peak to peak difference of predicted value. Variances increase monotonically beyond PC 6, noise dominates.

Validation results are shown. Solid line with no markers corresponds to simulation results for SHV prediction, showing potential prediction improvement in absence of experimental noise.

Figure 5(PM): Performance of the PLS models. a,b,c) Performance plot of the CH_4 (a), C_2H_6 (b) and N_2 (c) normal volume fraction prediction models, 3, 2 and 2 LVs were used respectively. d) Performance plot for the normal density prediction model. e) Performance plot for the Superior Heating Value prediction model. f) Performance plot of the Wobbe index prediction model. All plots show calibration points in grey and validation points in black. Straight lines are not fits; they depict the ideal performance line (unity slope line).

Figure 6(RE): Estimated SHV relative prediction error under different noise conditions. Relative error in SHV prediction as a function of different levels of added synthetic Gaussian noise characterized by a differential error factor. Different curves correspond to 2, 3, 4 and 6 latent variable prediction models. Relative error is expressed at the 95% (2σ) confidence interval. Error bars expressed at the 68% (1σ) confidence interval for clarity. Values estimated with 200 Monte Carlo runs.

Figure A1 (TD) (COLOR REPRODUCTION ON THE WEB, B&W IN PRINT): **Simulated temperature distribution across the gas volume**. Cross-section of the simulated temperature distribution across the gas volume. Graph has been obtained with ANSYS. Membrane width is 1500 µm. It can be seen that about 1 mm above the hotplate there is almost no temperature change. The sensor measurement seems to be mainly affected by $1mm^3$ of gas surrounding the hotplate.

TABLES PROVIDED IN A SEPARATE FILE.

ACKNOWLEDGMENT

ISP group is a consolidated Grup de Recerca de la Generalitat de Catalunya and has support from the *Departament d'Universitats, Recerca i Societat de la Informació de la Generalitat de Catalunya (expedient 2009 SGR 0753)*. This work has received support from the *Comissionat per a Universitats i Recerca del DIUE de la Generalitat de Catalunya* and the European Social Fund (ESF). The investigation has been also supported by the project TEC2004-07853-C02-01. S.U. acknowledges PhD grant from the Spanish Ministry of Education and Science. Kind support from ENAGAS in Barcelona, especially Manuel Mena, is acknowledged. Prof. Z. Karpas is acknowledged for his advice on structure and language.

REFERENCES

[1] P. Schley, M. Jaeschke, K. Altfeld, New technologies for gas quality determination, Proc 22nd World Gas Conference, Tokyo, June 2003, pp. 1-12.

[2] International Energy Agency, Natural Gas Distribution – Focus on western Europe, IEA publications, Paris, 1998, pp. 15-30.

[3] N. Makhoukhi, E. Péré, R. Creff, C. Pouchan, Determination of the composition of a mixture of gases by infrared analysis and chemometric methods, C. Journal of Molecular Structure, 744-747 (2005) 855-859.

[4] A. S. Brown, M. J. T. Milton, C. J. Cowper, G. D. Squire, W. Bremser, R. W. Branch, Analysis of natural gas by gas chromatography: Reduction of correlated uncertainties by normalisation, Journal of Chromatography, A, 1040(2004) 215-225.

[5] C. Rahmouni, M. Tazerout, O. Le Corre, Determination of the combustion properties of natural gases by pseudo-constituents, Fuel, 82(11) (2003) 1399-1409.

[6] International Energy Agency, 2010 Key World Energy Statistics, IEA publications, Paris, 2010, p. 60.

[7] International Organization for Standardization, ISO6976: Natural Gas – Calculation of calorific values, density, relative density and Wobbe index from composition, ISO 6976 International Standard.

[8] M. Malenshek, D. B. Olsen, Methane number testing of alternative gaseous fuels, Fuel, 88 (2009) 650-656.

[9] J. S. Stufkens, H. J. Bogaard, Rapid method for the determination of the composition of natural gas by gas chromatography, Analytical Chemistry, 47 (1975) 383-386.

[10] P. Ulbig, D. Hoburg, Determination of the calorific value of natural gas by different methods, Thermochimica Acta, 382(2002) 27-35.

[11] S. M. Donahue, C. W. Brown, B. Caputo, M.D. Modell, Near-infrared multicomponent analysis in the spectral and Fourier domains: energy content of high-pressure natural gas, Analytical Chemistry, 60 (1988) 1873-1878.

[12] P. Schley, Microsensors to Determine Superior Calorific value and Wobbe Number, Proc. Of the International Gas Research Conference, Amsterdam, November 2001, TP22/1-TP22/6.

[13] K. R. Wild, D. L. Ehrich, Energy metering technologies, Proc. Of the International Gas Research Conference, Amsterdam, November 2001, TO02/1-TO02/14.

[14] H. J. Panneman, C. W. Koreman, A.Kroon, H. Horstink, M. Jasechke, J. A. Schouten, J. P. J. Michels, A Fast Energy Measurement System Suitable for Process Control ans Off-shore Metering Applications, Proc. Of the International Gas Research Conference, Amsterdam, November 2001, TO03/1-TO03/12.

[15] E. R. Weaver, P. E. Palmer, Automatic Methods of Gas Analysis Depending on Thermal Conductivity, Journal of Industrial and Engineering Chemistry, 12 (1920) 359-366.

[16] C. Rahmouni, O. Le Corre, M. Tazerout, Online determination of natural gas properties, C. R. Mecanique, 331 (2003) 545-550.

[17] S. Udina, M. Carmona, G. Carles, J. Santander, L. Fonseca, S. Marco, A micromachined thermoelectric sensor for natural gas analysis: Thermal model and experimental results, Sensors and Actuators B: Chemical, B134 (2008) 551-558.

[18] G. Mandayo, Gas Detection by Semiconductor Ceramics: Tin Oxide as Improved Sensing Material, Sensor Letters, 5(2) (2007) 341-360.

[19] E. Comini, Metal oxide nano-crystals for gas sensing, Analytica Chimica Acta, 568(1-2) (2006) 28-40.

[20] K. Persaud, G. Dodd, Analysis of discrimination mechanisms in the mammalian olfactory system using a model nose, Nature 326(5881) (1982) 352-355

[21] J. W. Gardner, P. N. Barlett, A brief history of electronic noses, Sensors and Actuators B: Chemical, 18(1-3) (1994) 210-211.

[22] A. Hierlemann, R. Gutierrez-Osuna, Higher order chemical sensing, Chemical Reviews, 108(2) (2008) 563-613.

[23] S. Marco, A. Ortega, A. Pardo, J. Samitier, Gas identification with tin oxide sensor array and self-organizing maps: adaptive correction of sensor drifts, IEEE Transactions on Instrumentation and Measurement, 47(1) (1998) 316-321.

[24] T. Artursson, T. Eklov, I. Lundstrom, P. Martensson, M. Sjostrom, M. Holmberg, Drift correction for gas sensors using multivariate methods, Journal of chemometrics, 14(5-6) (2000) 711-723.

[25] A. Fort, M. Gregorkiewitz, N. Machetti, S. Rocchi, B. Serrano, L. Tondi, N. Ulivieri, V. Vignoli, G. Faglia, E. Comini, Selectivity enhancement of SnO2 sensors by means of operating temperature modulation, Thin Solid Films, 418(1) (2002) 2-8.

[26] V. Demarne, A. Grisel, An integrated low-power thin-film CO gas sensor on silicon, Sensors and Actuators, 13(4) (1988) 301-313.

[27] V. Demarne, S. Balkanova, A. Grisel, D. Rosenfeld, F. Lévy, Integrated gas sensor for oxygen detection, Sensors and Actuators B: Chemical, Volume 14, Issues 1-3, June 1993, Pages 497-498

[28] M. Graf, D. Barrettino, S. Taschini, C. Hagleitner, A. Hierlemann, H. Baltes Metal Oxide-Based Monolithic Complementary Metal Oxide Semiconductor Gas Sensor Microsystem, Analytical Chemistry, 76 (2004) 4437-4445.

[29] A. Heilig, N. Bârsan, U. Weimar, M. Schweizer-Berberich, J. W. Gardner, W. Göpel, Gas identification by modulating temperatures of SnO2-based thick film sensors, Sensors and actuators B: Chemical, 43(1-3) (1997) 45-51.

[30] H. D. Goeldner, B. Horn, T. Liedtke, W. R. Marx, W. Schaefer, Measuring component concentration in a gas blend , Parent number US4902138 (1990) 6 pp. CAN 112:210356

[31] A. Grunewald, Method and device for determining the gas concentrations in a gas mixture, Patent number US6688159 (2004), 20 pp. CAN 134:304801

[32] P. Tardy, J. Coulon, C. Lucat, F. Menil, Dynamic thermal conductivity sensor for gas detection, Sensors and Actuators, B: Chemical, B98(1) (2004) 63-68.

[33] S. Sorge, T. Pechstein, Fully integrated thermal conductivity sensor for gas chromatography without dead volume, Sensors and Actuators A: Physical, A63 (1997) 191-195.

[34] H.A. Daynes, Gas Analysis by Measurement of Thermal Conductivity, Cambridge Univ. Press, Cambridge, 1933.

[35] D. Puente, F. Gracia, I. Ayerdi, Thermal conductivity microsensor for determining the Methane Number of natural gas ,Sensors and Actuators B: Chemical, B110(2) (2005) 181-189.

[36] A. V. van Herwaarden, A. W. Sarro, Performance of integrated thermopile vacuum sensors, Journal of Physics E, 21 (1988) 1162-1167.

[37] S. Semancik, R. E. Cavicchi, M. C. Wheeler, J. E. Tiffany, G. E. Poirier, R. M. Walton, J. S. Suehle, B. Panchapakesan, D. L DeVoe, Microhotplate platforms for chemical sensor research, Sensors and Actuators B: Chemical, 77(1-2) (2001) 579-591.

[38] C. Calaza, E. Meca, S. Marco, M. Moreno, J. Samitier, L. Fonseca, I. Gracia, C. Cané, Assessment of the final metrological characteristics of a MOEMS-based NDIR spectrometer through system modeling and data processing , IEEE Sensors Journal 3(5) (2003) 587-594.

[39] A. Minakov, J. Morikawa, T. Hashimoto, H. Huth, C. Schick, Temperature distribution in a thin-film chip utilized for advanced nanocalorimetry, Measurement Science & Technology, 17(1) (2006) 199-207.

[40] M. Salleras, J. Palacin, M. Moreno, L. Fonseca, J. Samitier, S. Marco, A methodology to extract dynamic compact thermal models under time-varying boundary conditions: application to a thermopile based IR sensor, Microsyst. Technol., 12 (2005) 21-29.

[41] H. Baltes, O. Paul, O. Brand, Micromachined thermally based CMOS microsensors, Proceedings of the IEEE, 86(8) (1998) 1660-1678.

[42] P. Geladi, B. Kowalski, Partial Least Squares Regression: A tutorial, Analytica Chimica Acta, 185 (1986) 1-17.

[43] B. E. Poling, J.M. Prausnitz, J. P. O'Cornell, The properties of gases and liquids, 5th ed, McGraw-Hill, New York, 2001.

[44] National Institute of Standards and Technology (NIST), Chemical web book, http://webbook.nist.gov, last accessed November 2010.

[45] M. Matsumiya, W. Shin, F. Qiu, N. Izu, I. Matsubara, N. Murayama, Poisoning of platinum thin film catalyst by hexamethyldisiloxane (HMDS) for thermoelectric hydrogen gas sensor, Sensors and Actuators, B: Chemical, B96(3) (2003) 516-522.

[46] A. Vergara, E. Llobet, J. Brezmes, P. Ivanov, C. Cané, I. Gràcia, X. Vilanova, X. Correig, Quantitative gas mixture analysis using temperature-modulated micro-hotplate gas sensors: Selection

and validation of the optimal modulating frequencies, Sensors and Actuators B: Chemical, 123 (2007 1002-1016

[47] M. E. H. Amrani, R. M. Dowdeswell, P. A. Payne, K. C. Persaud, Pseudo-random binary sequence interrogation technique for gas sensors, Sensors and Actuators B: Chemical, 47(1-3) (1998) 118-124

[48] C. Calaza, Design, Modelling, Fabrication and Test of MOEMS for Optical Gas Detection, PhD Thesis, Universitat de Barcelona, Barcelona, 2003.

[49] D. G. Friend, J. F. Ely, H. Ingham, Thermophysical Properties of Methane, J. Phys. Chem. Ref. Data, 18(2) (1989) 583-638.

VITAE

Sergi Udina obtained the degree in electronic engineering by the *Universitat de Barcelona* in 2004, and the Master of Science degree in electronic engineering in 2007. His current investigation work is related to chemical and thermal sensors, multivariate calibration, signal processing and standard sensor interfacing basically including IEEE1451. He is currently pursuing his PhD degree at the *Departament d'Electronica* of the *Universitat de Barcelona,* and also performing research tasks at the IBEC.

Dr. Manuel Carmona obtained the PhD degree at the Universitat de Barcelona in 2000 in the field of modelling and simulation of MEMS. After that, he has worked at Infineon with thermo-mechanical issues of memory packages and at Seiko Epson with RF devices (resonators and microswitches). The main field of interest is the development of MEMS/NEMS, with strong focus on the use of modelling/simulation/test techniques.

Dr. Antonio Pardo received his diploma in physics 1991 and his PhD in 2000 from the University of Barcelona. During his PhD studies he worked in system identification with applications in gas sensor systems. Since 2005 he is associate professor at the University of Barcelona. His research interest focused on signal processing for gas sensors and pattern recognition as well as on hardware and software developments for electronic nose instrumentation.

Dr. J. Santander received the BS and PhD degrees in physics from the Autonomous University of Barcelona, Spain, in 1989 and 1996, respectively. He is currently at the Microelectronics National Centre in Barcelona that he joined in 1991 as a post-graduate student, becoming the person in charge of the electrical parametric characterization of different microelectronic technologies (CMOS, MCM,

Sensors, Microsystems). He is currently a full senior researcher working in areas related to microsystems, gas sensing applications and micro fuel cells.

Dr. Luis Fonseca received his BS and PhD degrees in physics from the Autonomous University of Barcelona in 1988 and 1992, respectively. In 1989, he joined the National Centre of Microelectronics as a post-graduate student, working till 1992 on the growth and characterization of thin dielectric films for VLSI and ULSI applications. In 2001, he joined the microsystems group as a full senior researcher being his actual research area focused on technological developments for gas sensing and more specifically on optical gas sensing.

Dr. Santiago Marco is an associate professor at the *Departament d'Electrònica of Universitat de Barcelona* since 1995. He received the BS degree in physics from the *Universitat de Barcelona* in 1988, and in 1993 his PhD from the *Departament de Física Aplicada i Electrònica*, *Universitat de Barcelona*. His current research interests are the modeling, simulation and test of microsystems and the development of intelligent gas measurement instruments based on soft-computing techniques.

Table(s)

TABLES

Calibration set							
n	**[CH_4] (%)**	**[C_2H_6] (%)**	**[N_2] (%)**	**[CO_2] (%)**	**SHV** ($MJ \cdot m^{-3}$)	**W** ($MJ \cdot m^{-3}$)	**d** ($MJ \cdot m^{-3}$)
1	100.0	0.0	0.0	0,0	39.831	53.469	0.717
2	84.7	8.0	6.1	1.22	39.357	49.538	0.816
3	81.8	8.1	8.9	1.22	38.234	47.678	0.831
4	80.8	11.8	6.1	1.22	40.496	50.229	0.840
5	78.0	11.9	8.9	1.22	39.371	48.398	0.856
6	84.0	8.1	6.1	1.78	39.139	49.039	0.824
7	81.2	8.1	8.9	1.78	38.012	47.198	0.839
8	81.4	12.0	6.2	0.42	40.827	50.901	0.832
9	77.4	11.9	8.9	1.78	39.152	47.931	0.863
10	82.6	10.0	7.5	0.0	39.865	50.040	0.821
11	79.6	10.0	7.5	2.99	38.687	47.486	0.858
12	91.1	0.0	7.4	1.50	36.272	46.822	0.776
13	71.1	19.9	7.5	1.50	42.262	50.579	0.903
14	88.5	10.1	0.0	1.50	42.263	53.743	0.800
15	73.6	10.0	14.91	1.50	36.305	44.029	0.879
16	81.0	10.0	7.5	1.50	39.274	48.740	0.839
17	100.00	0.0	0.0	0.0	39.831	53.469	0.717
18	100.00	0.0	0.0	0.0	39.831	53.469	0.717
19	73.6	10.0	14.92	1.50	36.300	44.021	0.879
20	100.00	0.0	0.0	0.0	39.831	53.469	0.717
Validation set							
21	84.7	8.1	6.1	1.22	39.365	49.548	0.816
22	81.8	8.1	8.9	1.22	38.238	47.682	0.831

23	80.8	11.9	6.1	1.22	40.502	50.236	0.840
24	78.0	11.9	8.9	1.22	39.377	48.407	0.856
25	84.0	8.1	6.1	1.78	39.144	49.045	0.824
26	81.2	8.1	8.9	1.78	38.017	47.203	0.839
27	80.3	11.9	6.1	1.78	40.281	49.750	0.848
28	77.4	11.9	8.9	1.78	39.154	47.934	0.863
29	82.6	10.0	7.5	0.0	39.865	50.041	0.821
30	79.6	10.0	7.5	3.00	38.688	47.488	0.858
31	91.1	0.0	74	1.50	36.274	46.824	0.776
32	71.1	19.9	7.5	1.50	42.267	50.583	0.903
33	88.5	10.0	0.0	1.50	42.264	53.742	0.800
34	81.1	10.0	7.5	1.50	39.276	48.745	0.839
35	81.8	8.1	8.9	1.22	38.238	47.682	0.831
36	87.5	9.3	3.2	0.00	41.392	52.842	0.793
37	95.3	2.7	2.1	0.00	39.825	52.450	0.745
38	93.2	4.6	1.1	1.09	40.337	52.406	0.766
FS	28.9	19.9	14.92	3	5.995	9.722	0.186

Table 1(XC). Experimental points used in the calibration and validation sets. Points 2 to 16 define a cubic centered experimental design, each point was duplicated, and pure methane was measured 4 times, since it was the point with a higher set point precision. Measurements 35 to 38 are approximations of real natural gas compositions from Holland, Norway, Russia and Algeria [5].Composition is expressed in %. Superior Heating Value, Wobbe Index and normal density (SHV, W, d respectively) are indicated. Row FS shows the full scale variation for each of the properties.

Property	Experimental (2-3LV)		Sim. 3LV		Sim. 6LV	
	Abs. Error	**R**	**Abs. Error**	**R**	**Abs. Error**	**R**
$[CH_4]$	0.60% (3 LV)	0.9990	0.25%	0.9998	0.12%	0.9999
$[C_2H_6]$	1.0% (2 LV)	0.9950	0.57%	0.9990	0.41%	0.9990
$[CO_2]$	1.3%(2 LV)	0.5660	1.1%	0.8350	0.58%	0.9470
$[N_2]$	0.90% (2 LV)	0.9900	0.73%	0.9940	0.22%	0.9995
	Rel. Error	**R**	**Rel. Error**	**R**	**Rel. Error**	**R**
d	0.82% (2 LV)	0.9970	0.54%	0.9990	0.30%	0.9999
H_S	1.0% (3 LV)	0.9920	0.68%	0.9970	0.43%	0.9990
W	1.5% (2 LV)	0.9860	1.0%	0.9980	0.72%	0.9970

Table 2(FM): Figures of merit of the PLS calibration. Values were obtained with a test set validation (see table 1(XC)) Simulation results provided were calculated in absence of experimental noise. *d* stands for normal density, H_S stands for superior heating value and *W* stands for Wobbe index.

Heater Voltage (V)→	**1**	**2**	**3**	**4**	**5**	**6**	**7**	**6.5**	**5.5**	**4.5**	**3.5**	**2.5**	**1.5**	**0.5**
Uncertainty sources affecting sensor measuring point repeatability (differential)														
Thermal noise (μV)	0.10	0.10	0.11	0.11	0.11	0.12	0.12	0.12	0.12	0.11	0.11	0.10	0.10	0.10
Voltmeter noise (μV)	7.8	10.1	13.8	18.8	25.0	32.2	40.2	36.1	28.5	21.7	16.1	11.7	8.7	7.8
T noise in V_{out}	See below													
V_{heater} noise in V_{out} (μV)	11	21	31	40	50	58	65	62	54	45	36	26	16	6
Uncertainty sources affecting gas mixture thermal conductivity (common mode)														
P noise in V_{out} (25mbar) (μV)[a]	0.5	1.5	1.5	2.0	4.5	6.0	5.0	6.0	8.0	4.5	5.0	3.5	2.5	1.0
T noise in V_{out} (0.2ºC) (μV)	-7	-26	-55	-91	-133	-168	-210	-188	-153	-110	-70	-38	-15	-2

[a]Apparently anomalous values are produced by large uncertainty in estimating dV_o/dP_a with the insufficiently accurate thermal conductivity measurements available (see ref [44], section A2).

Table 3(UR): Contribution of relevant experimental uncertainty sources to each of the components of the sensor output vector. Columns show the different vector components according to its corresponding heater voltage, they are ordered in time as they are presented to the sensor as shown in Figure 3(HW). Each noise contribution is different according to the voltage step considered, but relative magnitudes among noise sources are quite stable. Ambient temperature noise contributes to both uncertainty types.

Uncertainty source	Amb. Temp. variation (0.2ºC)	Amb. Pressure variation (25mbar)	V acquisition noise	Heater V noise	Thermal noise	B model (calibration error)	Expected prediction error (relative)
Density ($kg \cdot m^{-3}$)	$6.4x10^{-4}$	$6.2\ x10^{-6}$	$1.5\ x10^{-4}$	$2.5\ x10^{-4}$	$5.3\ x10^{-7}$	$6.2x10^{-3}$	$6.2\ x10^{-3}$ (0.76 %)
SHV ($MJ \cdot m^{-3}$)	$-5.8x10^{-2}$	$-8.2\ x10^{-3}$	$2.7\ x10^{-2}$	$4.8\ x10^{-2}$	$1.1\ x10^{-4}$	$5.3x10^{-1}$	$5.4x10^{-1}$ (1.4%)
W ($MJ \cdot m^{-3}$)	$-\ 1.1\ x10^{-1}$	$-9.5\ x10^{-3}$	$2.4\ x10^{-2}$	$4.35\ x10^{-2}$	$1.0\ x10^{-4}$	1.10	1.12 (2.4%)
$[CH_4]$	$-7.0x10^{-4}$	$-5.9x10^{-4}$	$2.3x10^{-3}$	$4.5x10^{-3}$	$1.3x10^{-5}$	$0.75x10^{-2}$	0.76%
$[C_2H_6]$	$-1.8x10^{-4}$	$-1.10x10^{-4}$	$4.7x10^{-4}$	$8.3x10^{-4}$	$1.9x10^{-6}$	$1.0x10^{-2}$	1.0%
$[CO_2]$	$4.8x10^{-5}$	$-2.6x10^{-6}$	$2.1x10^{-5}$	$3.6x10^{-5}$	$7.7x10^{-8}$	$1.28x10^{-2}$	1.3%
$[N_2]$	$1.3x10^{-3}$	$1.25x10^{-4}$	$3.4x10^{-4}$	$6.2x10^{-4}$	$1.4x10^{-6}$	$0.9x10^{-2}$	1.1%

Table 4(PU): Totalized contribution of the uncertainty sources to the prediction error. Results estimated with Monte Carlo analysis and adding synthetic Gaussian noise to the experimental measurements. B model uncertainty is the calibration error, which is affected by $\boldsymbol{\varepsilon_x}$ and $\boldsymbol{\varepsilon_y}$ uncertainties. Results are consistent with experimental validation result

Figure 1_rev
Click here to download high resolution image

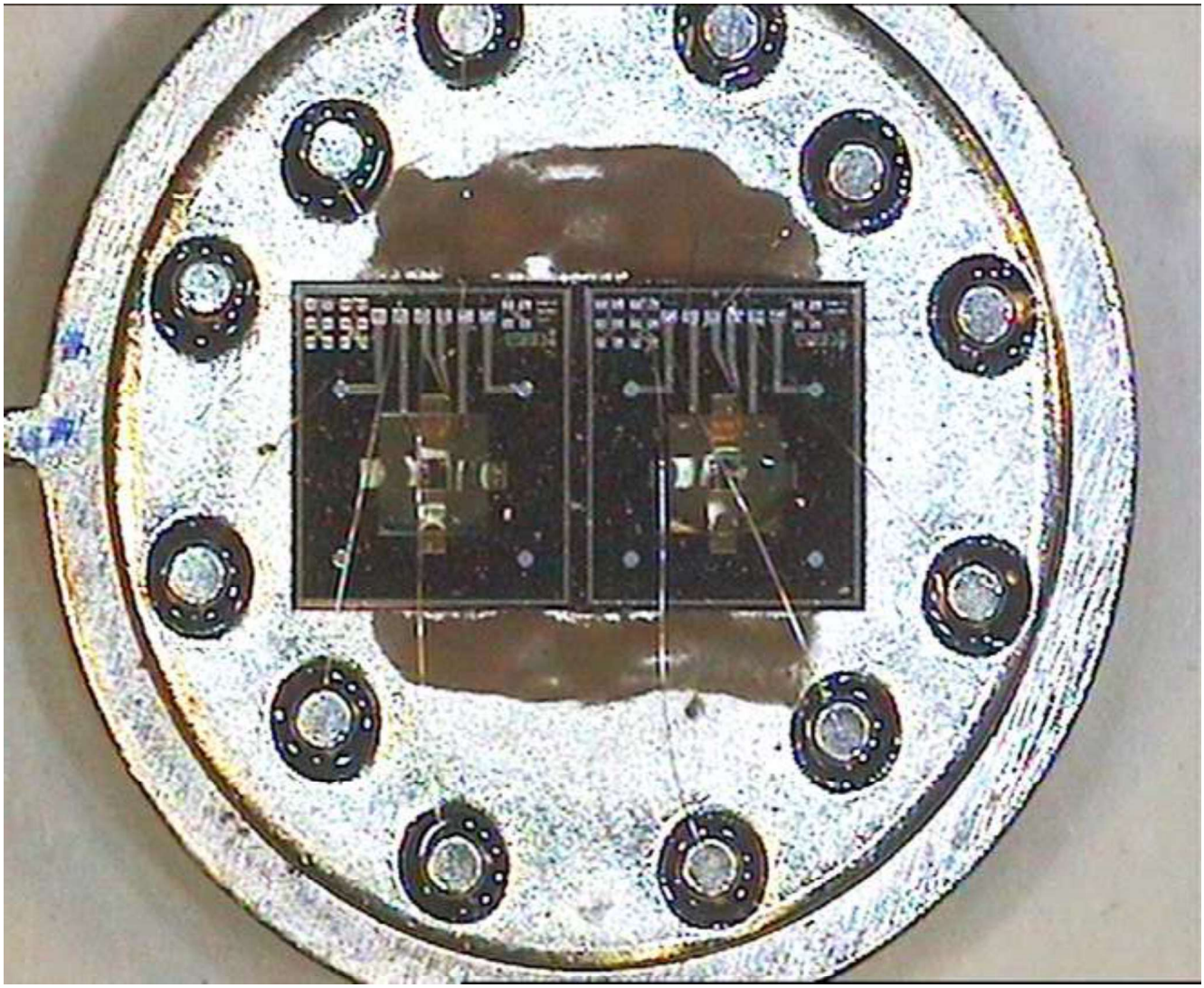

Figure 2
Click here to download high resolution image

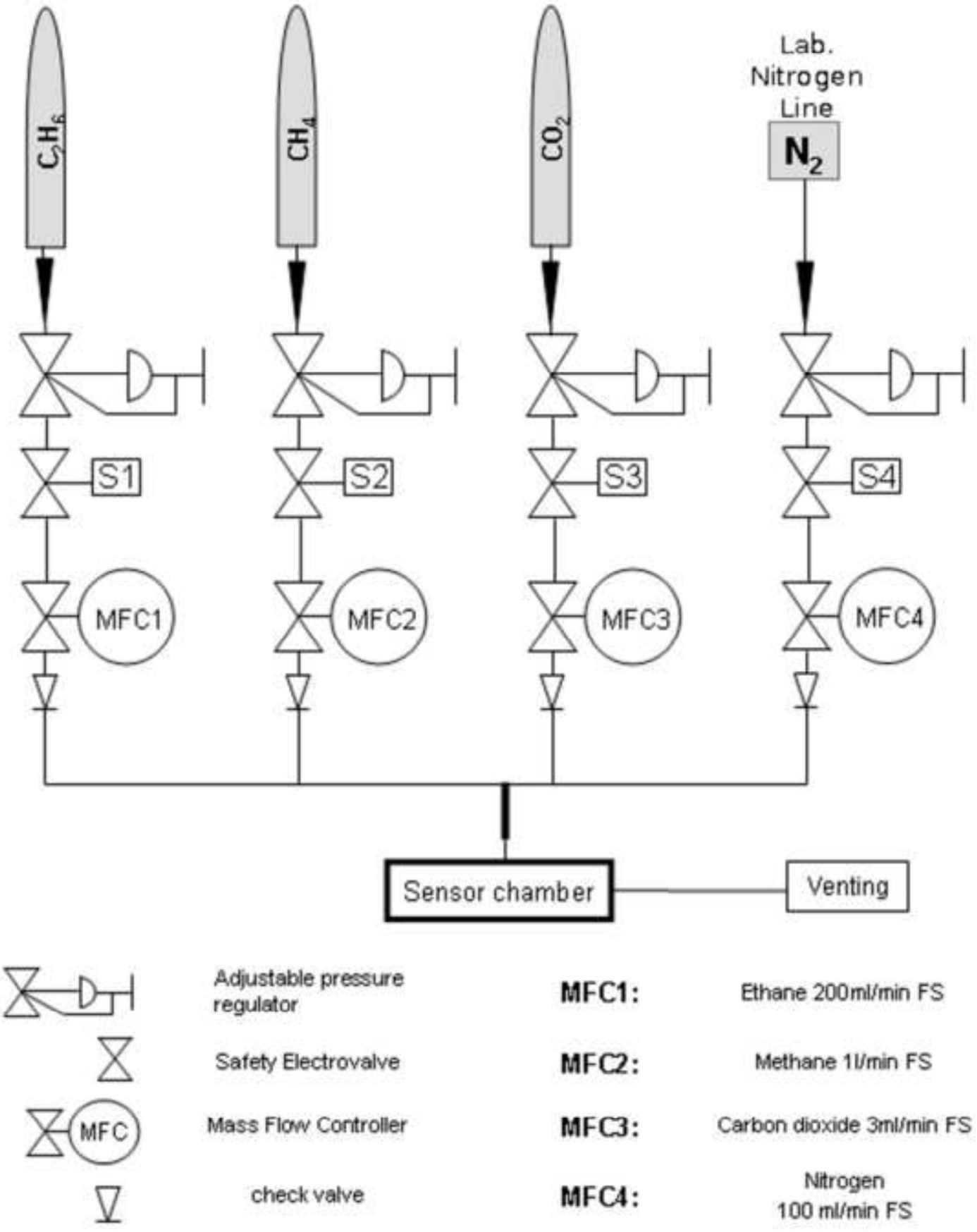

Figure 3
Click here to download high resolution image

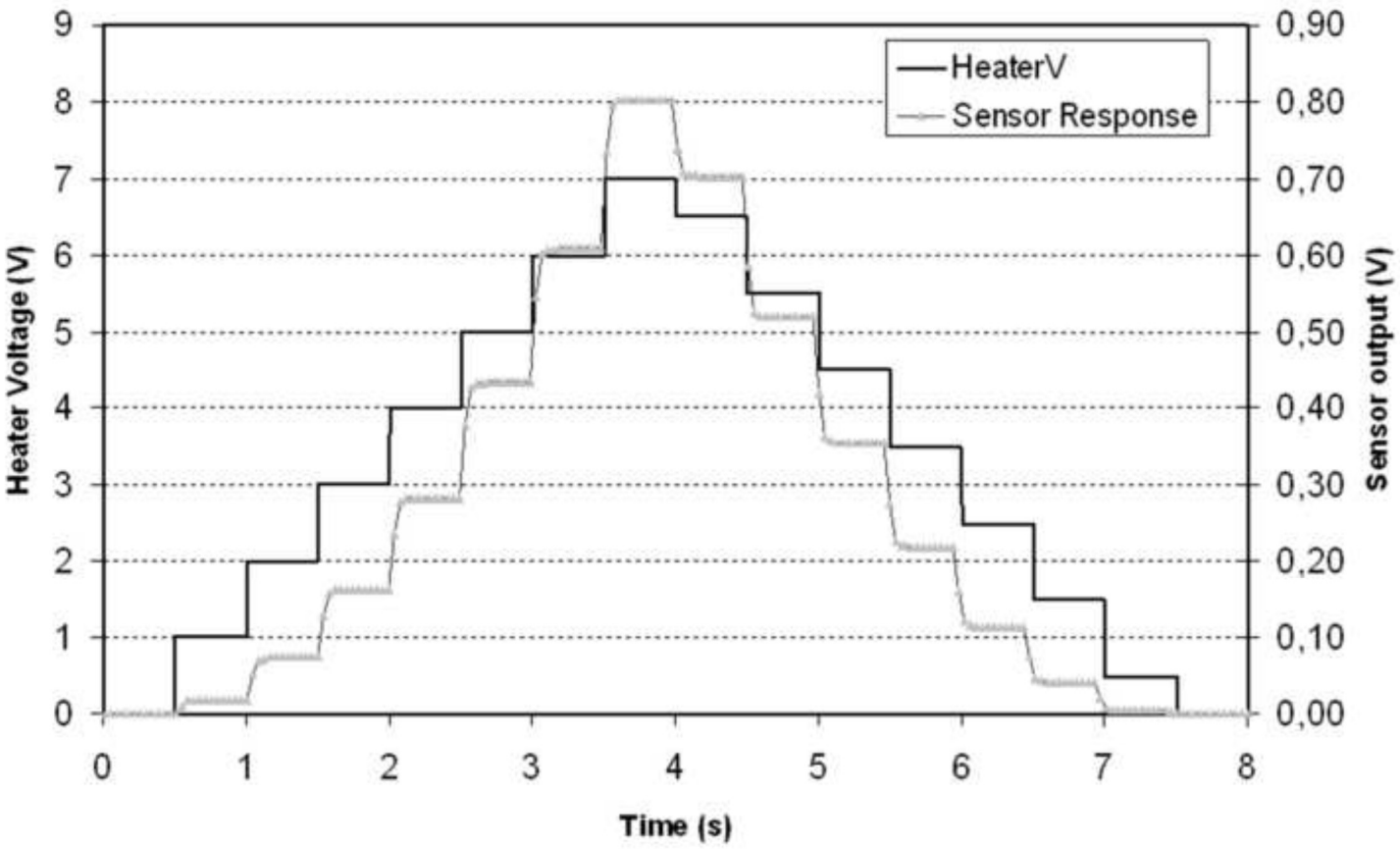

Figure 4
Click here to download high resolution image

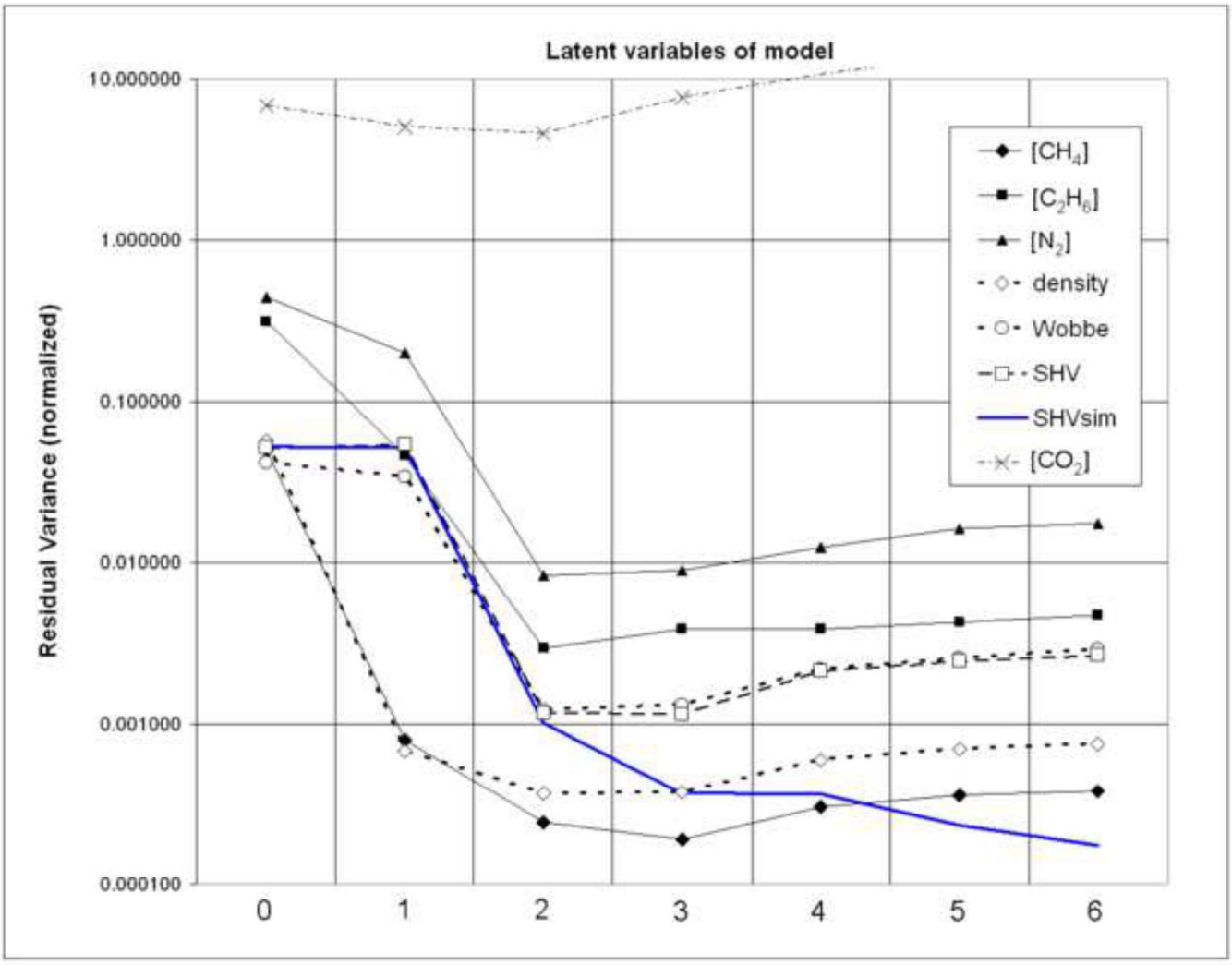

Figure 5
Click here to download high resolution image

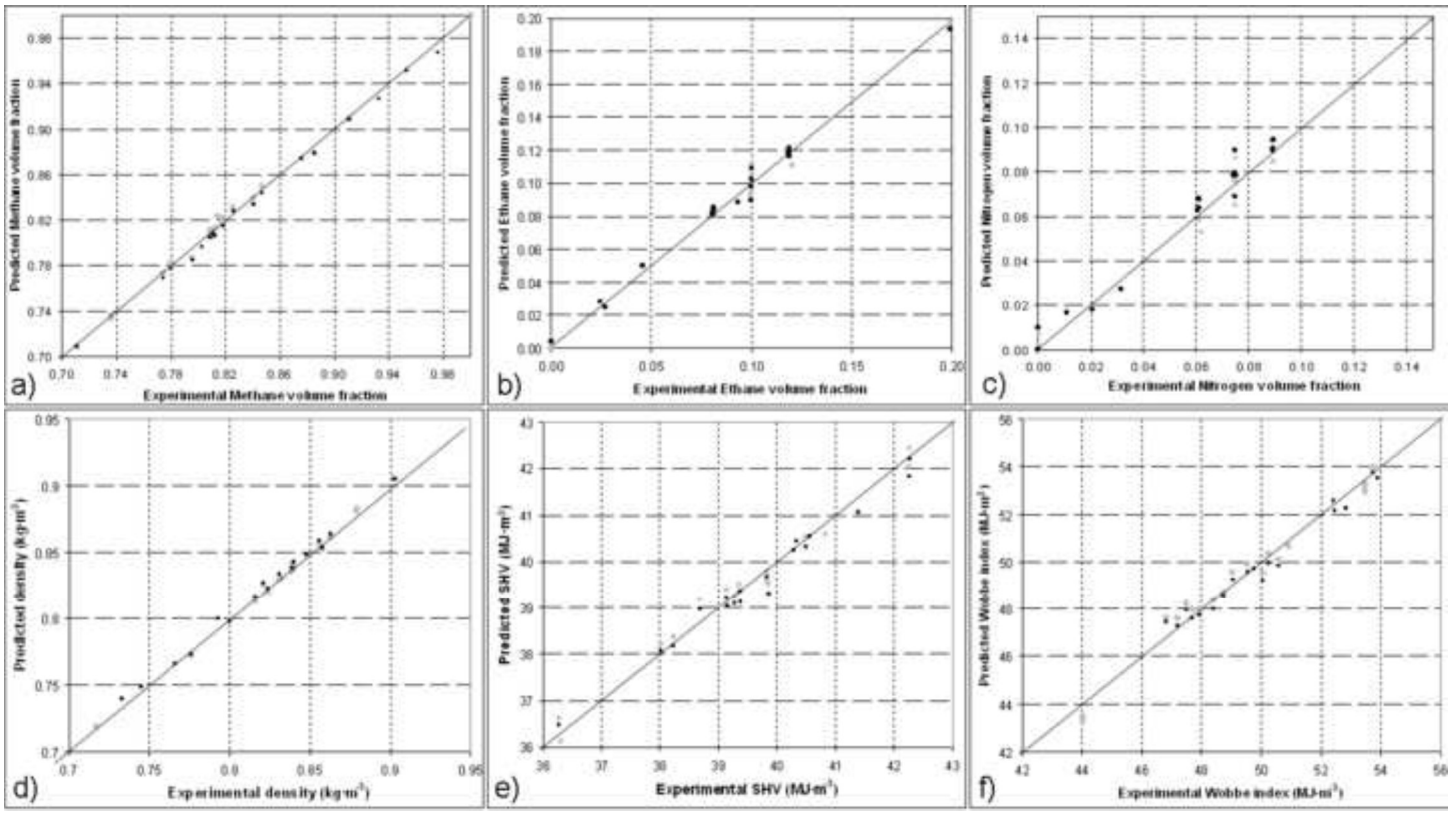

Figure 6
Click here to download high resolution image

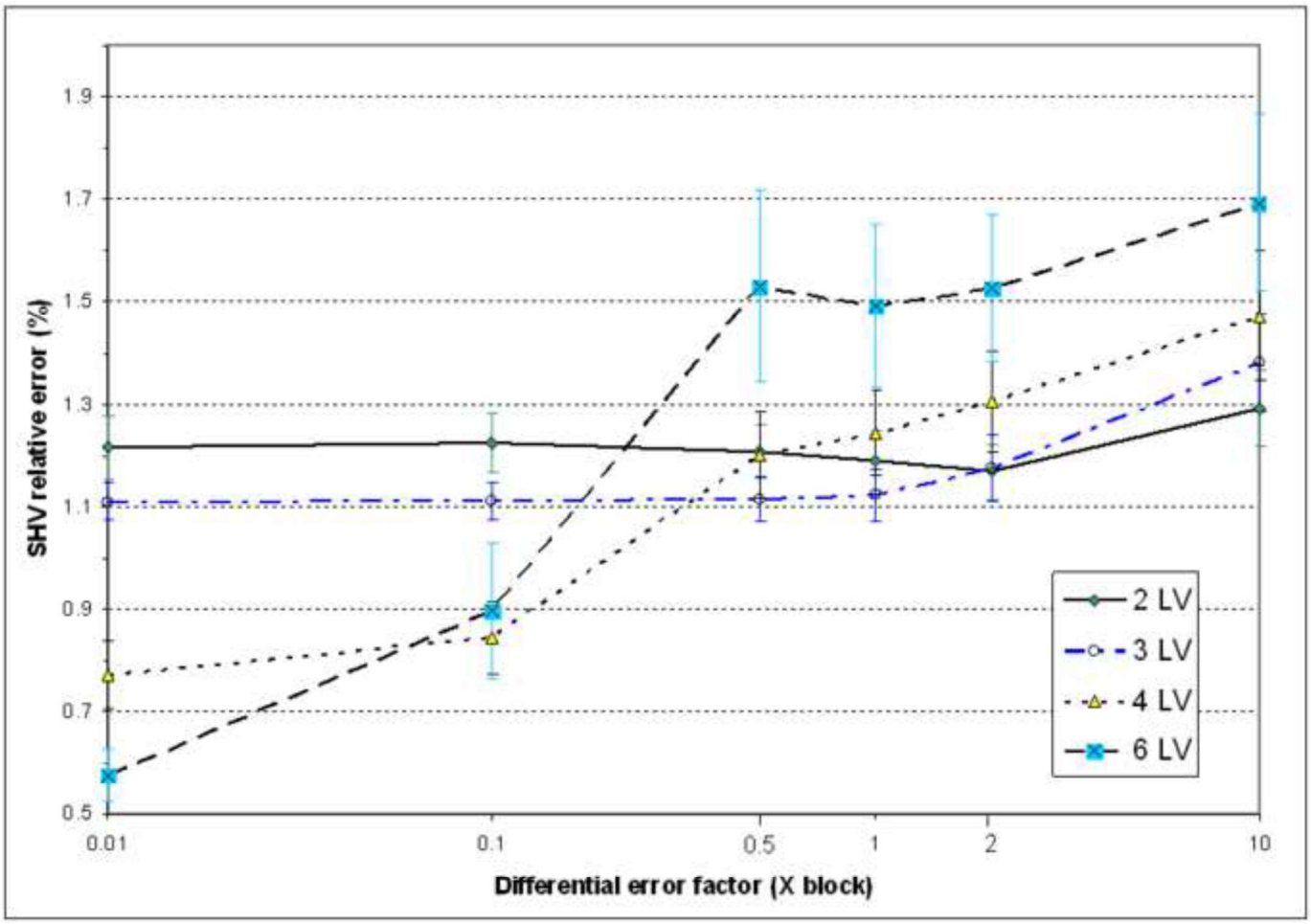

Figure A1
Click here to download high resolution image